Springer

KSME

Journal of Mechanical Science and Technology 30 (9) (2016) 4031~4042
www.springerlink.com/content/1738-494x(Print)/1976-3824(Online)
DOI 10.1007/s12206-016-0816-z

Dynamic characteristics of rotating pretwisted clamped-clamped beam under thermal stress †

Bo Zhang[1], Yueming Li[1,*] and Wei-Zhen Lu[2]

[1]*State Key Laboratory for Strength and Vibration of Mechanical Structures, Shaanxi Key Laboratory of Environment and Control for Flight Vehicle, School of Aerospace, Xi'an Jiaotong University, China*
[2]*Department of Civil and Architectural Engineering, City University of Hong Kong, China*

(Manuscript Received May 11, 2015; Revised May 7, 2016; Accepted May 10, 2016)

Abstract

Effects of thermal stress on the vibration characteristics, buckling limit and critical speed of a rotating pretwisted beam clamped to rigid hub at a stagger angle were investigated. By considering the work done by thermal stress, the thermal influence on stiffness matrix was introduced in the dynamic model. The motion equations were derived based on Lagrange equation by employing three pure Cartesian deformation variables combined with nonlinear von Karman strain formula. Numerical investigations studied the modal characteristics of the beam. Numerical results calculated from a commercial finite element code and obtained with the present modeling method were in good agreement with the previous results reported in the literature. The combined softening effects due to the thermal stress and the rotation motion were observed. Furthermore, it is shown that the inclusion of thermal stress is necessary for blades operating under a high temperature field. Buckling thermal loads and the critical rotating speed were calculated through solving the corresponding nonlinear equations numerically, and some pertinent conclusions are outlined. It is also found that the peak value position of the first mode shape approaches to the tip of blade with the increment of rotating speed and hub radius. However, the variation in the environment temperature causes only a slight alteration in the mode shape.

Keywords: Rotating pretwisted shrouded blade; Thermal environment; Critical rotating speed; Buckling; Natural frequencies; Mode shape

1. Introduction

The blade is a vital part of a turbo-machine, and its dynamic strength is of considerable importance. It is well-known that the turbo-machine blades are exposed under a severe thermal load, especially in gas turbines. Furthermore, in order to improve the efficiency, the operating temperature is desired to be raised to an even higher level. To some extent, the appendages (i.e., outer shroud) could prevent fatigue failures of turbo-machine blades. However, at the same time, the thermal expansion is restricted by the friction between the outer shrouds during rotating. As a result, thermal stress is produced throughout the blade. To design such structures properly, we need a better understanding of the dynamic characteristics of blades under thermal environment to avoid some undesirable problems such as resonance phenomena and buckling instability.

Generally, a turbo-machine blade is idealized as a tapered pretwisted rotating beam in theoretical research works. The modeling method and vibration analysis of a rotating flexible beam have attracted widespread attention. An extensive list of related papers was well reviewed by Rao [1]. Without considering the thermal environment, many investigations about the vibration characteristics of blades under rotating and non-rotating conditions have been carried out during past two decades. The upper bound for the *n*th natural frequency of an exponentially tapered beam under rotation was determined theoretically by Sahu [2]. Yoo et al. [3] established a model for pretwisted rotating blades with a concentrated mass and analyzed the vibration characteristics of a rotating blade. Ramesh and Rao [4] extended Yoo's modeling method for estimating natural frequencies of a functionally graded rotating pre-twisted cantilever beam. Piovan and Sampaio [5] used finite element method and Hamilton's principle to examine nonlinear dynamics of a rotating beam made of functionally graded materials. Banerjee [6-9] applied the dynamic stiffness method combined with the Wittrick and Williams algorithm to study the modal characteristics of rotating tapered Euler-Bernoulli, Timoshenko and Rayleigh beams, respectively. Chu et al. [10] studied the impact of vibration characteristics on a shrouded blade under wake flow excitations. Chiu and Yang [11] emphasized the coupling behavior between shaft-torsion and blade-bending with a rotor system composed of

*Corresponding author. Tel.: +86 2982668340, Fax.: +86 2982669044
E-mail address: liyueming@mail.xjtu.edu.cn
† Recommended by Editor Yeon June Kang

shaft, multi-disk and blades packeted by lacing. Zhang and Li [12] observed a series of perturbation frequency components in dynamic response of a rotating shaft with a breathing transverse crack. Khan and Parhi [13] used the radial basis function neural network technique to detect the transverse cracks in composite beam. Yao et al. [14, 15] adopted Galerkin's approach and perturbation method to study the nonlinear dynamic response of the rotating pretwisted thin-walled blade with varying speed. Hamdan and El-Sinawi [16] established the Euler-Lagrange equations of the nonlinear vibrations of a slender flexible rotating arm attached to a rotating hub at a stagger angle. Kaya and Ozgumus [17] performed free vibration analysis of a uniform, rotating, cantilever Timoshenko beam featuring coupling between flapwise bending and torsional vibration. For the topic of the dynamic stability of beam, there have been also some papers available in the literature. Sakar and Sabuncu [18] pointed out the effects of coupling due to shear center distance from the centroid, pretwist angle, rotating speed, stagger angle on the static buckling loads and dynamic instability regions of an aerofoil blade. Lee [19] studied buckling and dynamic stability of spinning pretwisted beams under compressive axial loads. Badagi and Ganesan [20] investigated the effects of the ratio of the width of the thick section to thin section, boundary conditions, effects of axial and compressive force on natural frequency and buckling analysis. Fu et al. [21] provided a set of analytical methods to solve the thermal buckling of composite beams. Ranjbaran et al. [22] investigated the buckling behavior of sandwich plate using layer-wise method.

A few research works consider the thermal environment when investigating the dynamic behavior of a rotating blade. Considering transient thermal effect, Johnston and Thornton [23] investigated the dynamic performance of a flexible cantilevered hub-appendage with tip mass with a geometric linear model. Saniei and Luo [24] presented the dynamic responses for the free vibration heated rotating disk analytically. Oguamanam and Hansen [25] observed the nonlinear response of a composite laminated panel that is suddenly exposed to a heat flux. Liu and Lu [26] developed a geometric nonlinear hybrid coordinate formulation for rigid-flexible coupling dynamical analysis of rotating hub-beam applied with thermal load. In these papers, the authors concentrated just on the transient response of a rotating structure under a thermal environment. Tomar and Jain [27, 28] determined the thermal effect on frequencies of wedged-shaped and pretwisted beams. Song et al. [29] developed a theory for the dynamic analysis of a rotating pretwisted thin-walled beam under a temperature field. Na et al. [30] addressed the problem of bending vibration, dynamic response of a rotating blade impacted by a blast and operating in a temperature field. Librescu et al. [31] considered the modeling and free vibration of pre-twisted rotating blades made of functionally graded materials under a high-temperature environment. The thermal degradation of material properties on eigen frequencies was presented by the authors. These papers provide a straightforward approach to introduce the thermal effect into the dynamic characteristics of rotating structure. This approach is assuming the mechanical properties of constituent materials are temperature-dependent. However, the research on the influence of thermal stress on the modal characteristics and buckling limit for pretwisted rotating hub-beam is insufficient. This paper makes a modest attempt to supplement this topic. Our attention is restricted to the effects of thermal stress on dynamic behavior and stability of the rotating blade.

We assume the shrouded blade to be a rotating pretwisted beam clamped on both ends. The geometric nonlinearity of the beam is considered through the von Karman strain-displacement formula. The motion equations including the effect of thermal stress are established by applying Lagrange equation. The equations are transformed into a dimensionless form through introducing a set of dimensionless parameters. The accuracy of the model proposed in this study is validated by comparing the natural frequency to that computed from a commercial finite-element code. The effects of environment temperature and rotating motion on the natural frequencies, modal shape, buckling limit and critical speed for the pretwisted shrouded blade are investigated. Some new phenomena are observed through numerical calculations.

2. Mathematic modeling

2.1 Description and assumption of the model

The configuration of a pretwisted shrouded blade is depicted in Fig. 1. The pretwisted blade is assembled on a rigid hub with a stagger angle. The hub, with radius r, is rotating about its central axis at a constant speed of Ω. The whole system is operating under a uniform temperature rise (ΔT) from stress free status.

Two types of coordinate system, the global inertial coordinate XYZ and the rotating blade coordinate xyz, are considered (see Fig. 2). Associated with these two coordinate systems xyz and XYZ, we define the unit vectors i, j, k and I, J, K, respectively. The coordinate xyz is attached at the center of root section and rotates with the blade. The axis x is along the undeflected blade centroid axes, axis y is in the rotation plane of the blade, and axis z is parallel to the axis Z in the inertial coordinate. The axes y_r and z_r denote the two principal axes of root section. Similarly, y_tz_t and y_pz_p represent those of tip section and a general section, respectively. Point P is an arbitrary point placed on the general section. Ψ denotes the blade stagger angle. The pretwist angle between the root section and the general section is θ, which is a function of the total pretwist angle Θ and the position of the section. The variables u_1, u_2 and u_3 describe the axial, chordwise and flapwise deformation components of the points on the centroid axes of the blade, respectively. In this study, it is assumed that the hub and the outer shroud are a rigid body and the blade is clamped between them. This geometric arrangement leads to the possibility of buckling instability. With Euler-Bernoulli assumption, the effects of shear deformation and rotary inertia are not

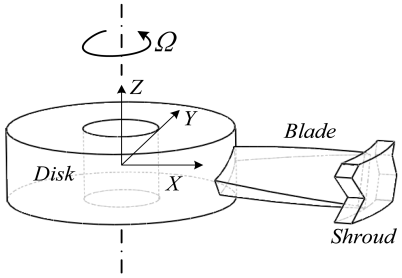

Fig. 1. The configuration of a pretwisted shrouded blade.

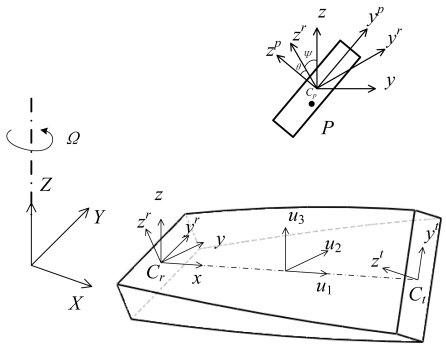

Fig. 2. The coordinate systems and a general cross-section.

taken into account. The material of the beam is homogeneous and isotropic. The variation of pretwist angle is uniform along the longitudinal axis.

2.2 Kinetic and potential energy of the system

The kinetic energy of the blade is given by the following integration:

$$KE = \frac{1}{2}\int_0^L \rho A \mathbf{v}_P^T \mathbf{v}_P \mathrm{d}x \,, \tag{1}$$

where ρ is the density; A is the area of cross section; L is the length of the blade; v_P is the velocity vector of material point. From the kinematics analysis, v_P could be written as follows [32]:

$$\mathbf{v}_P = \left(\dot{u}_1 - \Omega u_2\right)\mathbf{i} + \left(\dot{u}_2 + \Omega\left(r + x + u_1\right)\right)\mathbf{j} + \dot{u}_3\mathbf{k} \,. \tag{2}$$

Considering the thermal environment, the potential energy of the system consists of three parts: The mechanical deformation energy U_σ, thermal stress potential energy U_T and the potential energy U_{as} due to the axis shortening via transverse deformations and the rotational inertial forced. So the total potential energy is:

$$PE = U_\sigma + U_T + U_{as} \,. \tag{3}$$

With Euler-Bernoulli assumption, the displacement components of the material point P in the rotating frame should follow the following form:

$$u_x(x,y,z,t) = u_1(x,t) - y\frac{\partial u_2(x,t)}{\partial x} - z\frac{\partial u_3(x,t)}{\partial x} \,, \tag{4}$$

$$u_y(x,y,z,t) = u_2(x,t) \,, \tag{5}$$

$$u_z(x,y,z,t) = u_3(x,t) \,. \tag{6}$$

The geometric nonlinearity is considered through von Karman strain-displacement formula.

$$\varepsilon_x = \frac{\partial u_x}{\partial x} + \frac{1}{2}\left(\frac{\partial u_y}{\partial x}\right)^2 + \frac{1}{2}\left(\frac{\partial u_z}{\partial x}\right)^2 \,. \tag{7}$$

Ignoring the third and higher order terms of the displacement variables, the mechanical deformation energy can be expressed as:

$$\begin{aligned} U_\sigma &= \frac{1}{2}E\int_V \left(\frac{\partial u_1}{\partial x}\right)^2 - 2y\frac{\partial^2 u_2}{\partial x^2}\frac{\partial u_1}{\partial x} - 2z\frac{\partial^2 u_3}{\partial x^2}\frac{\partial u_1}{\partial x} + y^2\left(\frac{\partial^2 u_2}{\partial x^2}\right)^2 \\ &\quad + 2yz\frac{\partial^2 u_2}{\partial x^2}\frac{\partial^2 u_3}{\partial x^2} + z^2\left(\frac{\partial^2 u_3}{\partial x^2}\right)^2 \mathrm{d}V + (\text{higher order terms}) \\ &\doteq \frac{1}{2}\int_0^L EA\left(\frac{\partial u_1}{\partial x}\right)^2 \mathrm{d}x + \frac{1}{2}\int_0^L EI_3\left(\frac{\partial^2 u_2}{\partial x^2}\right)^2 \mathrm{d}x \\ &\quad + \int_0^L EI_{23}\frac{\partial^2 u_2}{\partial x^2}\frac{\partial^2 u_3}{\partial x^2}\mathrm{d}x + \frac{1}{2}\int_0^L EI_2\left(\frac{\partial^2 u_3}{\partial x^2}\right)^2 \mathrm{d}x \end{aligned} \tag{8}$$

in which E is the Young's modulus of elasticity, and

$$I_2 = \int_{A_P} z^2 \mathrm{d}A,\ I_3 = \int_{A_P} y^2 \mathrm{d}A,\ I_{23} = \int_{A_P} yz \mathrm{d}A \tag{9}$$

are the second moments of area and the mixed second moment of area of the general section A_P in the rotating frame. They can be calculated with rotation transform matrix.

$$I_2(x) = \frac{I_2^* + I_3^*}{2} + \frac{I_2^* - I_3^*}{2}\cos\left[2(\theta + \Psi)\right], \tag{10a}$$

$$I_3(x) = \frac{I_2^* + I_3^*}{2} - \frac{I_2^* - I_3^*}{2}\cos\left[2(\theta + \Psi)\right], \tag{10b}$$

$$I_{23}(x) = \frac{I_2^* - I_3^*}{2}\sin\left[2(\theta + \Psi)\right]. \tag{10c}$$

Upon the assumption of linear variation, the pretwist angle θ could be expressed as:

$$\theta = \frac{x}{L}\Theta \,. \tag{11}$$

The potential energy due to thermal stress is numerically equal to the work done by it.

$$U_T = -\int_0^L N_T \left[\frac{\partial u_1}{\partial x} + \frac{1}{2}\left(\frac{\partial u_2}{\partial x}\right)^2 + \frac{1}{2}\left(\frac{\partial u_3}{\partial x}\right)^2 \right] \mathrm{d}x + \int_0^L M_{Tz} \frac{\partial^2 u_2}{\partial x^2} \mathrm{d}x + \int_0^L M_{Ty} \frac{\partial^2 u_3}{\partial x^2} \mathrm{d}x \tag{12}$$

where

$$N_T = \int_A E\alpha\Delta T(y,z)\,\mathrm{d}A,\ M_{Tz} = \int_A E\alpha\Delta T(y,z) y\,\mathrm{d}A,\ M_{Ty} = \int_A E\alpha\Delta T(y,z) z\,\mathrm{d}A \tag{13}$$

are the thermal internal force and two thermal bending moments, in which α is the coefficient of thermal expansion.

The neutral axis shortening due to transverse deformation and axial inertial force results in a contribution to the system elastic potential energy known as the axial shortening potential energy [33-35]. The amount of axial shortening due to the transverse deformations reads:

$$\mathrm{d}s_b = -\left[\frac{1}{2}\left(\frac{\partial u_2}{\partial x}\right)^2 + \frac{1}{2}\left(\frac{\partial u_3}{\partial x}\right)^2 \right] \mathrm{d}x . \tag{14}$$

Considering the clamped-clamped boundary condition and equilibrium equation, the axial inertial force due to the rotational motion of clamped beam can be calculated in the form:

$$F_P = \frac{1}{6}\rho A\Omega^2 \left(L^2 - 3x^2\right) + \frac{1}{2}\rho A\Omega^2 r\left(L - 2x\right). \tag{15}$$

Then, the axial shortening potential energy is calculated as follow expression:

$$U_{as} = \int F_P \mathrm{d}s_b . \tag{16}$$

2.3 Equations of motion

The Assumed modes method (AMM) is used for discretizing the three displacement components. The displacement functions are separated into products of spatial and temporal functions.

$$u_i(x,t) = \sum_{j=1}^{n_i} \phi_{ij}(x) q_{ij}(t) \ . \tag{17}$$

For displacement u_i (i =1, 2, 3), n_i is number of assumed modes, $q_{ij}(t)$ are generalized coordinates and $\phi_{ij}(x)$ are totally unrestricted spatial functions, respectively. In the present study, the eigenfunctions of a clamped-clamped beam are applied.

The kinetic and potential energy expressions obtained in previous section are used to develop the equation of motion with Lagrange equation.

$$\frac{\mathrm{d}}{\mathrm{d}t}\frac{\partial \tilde{L}}{\partial \dot{q}} - \frac{\partial \tilde{L}}{\partial q} = 0 , \tag{18}$$

in which $\tilde{L}$ is Lagrangian function. Then we get the equation of motion in matrix form.

$$\mathbf{M}\ddot{\mathbf{q}} + \mathbf{C}\dot{\mathbf{q}} + \mathbf{K}\mathbf{q} = \mathbf{Q} . \tag{19}$$

In which

$$\mathbf{M} = \begin{bmatrix} M^{11} & 0 & 0 \\ 0 & M^{22} & 0 \\ 0 & 0 & M^{33} \end{bmatrix} \tag{20}$$

$$\mathbf{C} = \begin{bmatrix} 0 & -2\Omega M^{12} & 0 \\ 2\Omega M^{21} & 0 & 0 \\ 0 & 0 & 0 \end{bmatrix} \tag{21}$$

$$\mathbf{K} = \begin{bmatrix} K^S - \Omega^2 M^{11} & 0 & 0 \\ 0 & K^{B2} - \Omega^2 M^{22} + K^{\Omega 2} - K^{T2} & K^{B23} \\ 0 & K^{B32} & K^{B3} + K^{\Omega 3} - K^{T3} \end{bmatrix} \tag{22}$$

$$\mathbf{Q} = \left[Q_1, Q_2, Q_3\right]^{\mathrm{T}} , \tag{23}$$

are the mass matrix, damping matrix, stiffness matrix and load vector, respectively. These matrices and vector are listed in detailed in Appendix A. Special attention is paid to the stiffness matrix. K^S is the stretch stiffness; K^{B2} and K^{B3} stand for the stiffness due to bending deformations; $\Omega^2 M^{11}$ and $\Omega^2 M^{22}$ are the spin softening terms in the plane of rotation; $K^{\Omega 2}$ and $K^{\Omega 3}$ stand for the centrifugal stress effect on the two bending vibrations; the terms K^{T2} and K^{T3} denote the thermal softening effect on the two bending vibrations; K^{B32} and K^{B23} represent the coupling effects between the flapwise and chordwise vibrations resulting from the nonzero pretwist angle and stagger angle.

The skew symmetric matrix C represents the Coriolis effect of the rotating beam, which introduces the coupling terms between axial and bending vibrations. As Yoo [36] explained, for Euler-Bernoulli beam, the first axial natural frequency is far from the bending natural frequencies. So the coupling effects could be ignored. To study the free vibration of the rotating beam, the load vector is omitted. Consequently, the Eq. (19) is reduced to:

$$\begin{bmatrix} M^{22} & 0 \\ 0 & M^{33} \end{bmatrix} \begin{Bmatrix} \ddot{q}_2 \\ \ddot{q}_3 \end{Bmatrix} + \begin{bmatrix} K^{B2} - \Omega^2 M^{22} + K^{\Omega 2} - K^{T2} & K^{B23} \\ K^{B32} & K^{B3} + K^{\Omega 3} - K^{T3} \end{bmatrix} \begin{Bmatrix} q_2 \\ q_3 \end{Bmatrix} = \mathbf{0} . \tag{24}$$

For the sake of generality, following dimensionless variables are introduced.

$$\tau = t\Big/\sqrt{\frac{\rho AL^4}{EI_3^*}},\ \chi = \frac{x}{L},\ \xi_{ij} = \frac{q_{ij}}{L},\ \kappa = \left(\frac{h}{w}\right)^2 = \frac{I_2^*}{I_3^*},$$
$$\mu = \left(\frac{L}{w}\right)^2,\ \delta = \frac{r}{L},\ \gamma = \Omega\sqrt{\frac{\rho AL^4}{EI_3^*}},\ \varepsilon_T = \alpha\Delta T, \tag{25}$$
$$\varphi_i(\chi) = \phi_i(\chi L) = \phi_i(x), (i = 1,2,3).$$

The parameters κ, μ, δ, γ and ε_T represent height to width ratio, length ratio, hub radius ratio, rotating speed ratio and dimensionless temperature (thermal strain), respectively. The functions $\varphi_i(\chi)$ is the shape function of the dimensionless position χ. Applying these parameters, the dimensionless equation of motion is obtained.

$$\bar{\mathbf{M}}\ddot{\xi} + \bar{\mathbf{K}}\xi = \mathbf{0}. \tag{26}$$

The dimensionless matrices and elements are documented in Appendix A.

It is assumed that the solution is of a harmonic form $\xi(\chi,\tau) = X(\chi)exp(i\omega\tau)$. The vibration characteristics could be obtained by solving the corresponding eigenvalue problem. Obviously, the base frequency of the pretwisted rotating beam is an implicit nonlinear function of system parameters and could be written as:

$$\omega_{base} = \omega_{base}(\Psi, \Theta, \kappa, \mu, \delta, \gamma, \varepsilon_T). \tag{27}$$

In the buckling limit, note that the term $exp(i\omega\tau)$ grows unbounded with increasing time τ, when $\omega^2 < 0$. So the stability limit is the value of load (such as environment temperature, rotating speed) which results in zero base frequency, i.e.,

$$\omega_{base}(\Psi, \Theta, \kappa, \mu, \delta, \gamma, \varepsilon_T) = 0. \tag{28}$$

This is equivalent to setting the determinant of stiffness matrix to zero. When all other variables are set to a fixed value, the dimensionless buckling temperature ε_{Tb} and dimensionless buckling rotating speed γ_b could be obtained.

In addition, when the rotating speed of the blade is close to a certain natural frequency of the rotating beam, the resonance phenomenon will appear. Catastrophic failures often occur at these critical rotating speeds. Hence, the critical rotating speed should be given enough attention during designing the rotating blade. Similarly, the first critical rotating speed γ_c could be calculated from solving following nonlinear equation

$$\omega_{base}(\Psi, \Theta, \kappa, \mu, \delta, \gamma, \varepsilon_T) - \gamma = 0. \tag{29}$$

It is impossible to analytically evaluate these nonlinear Eqs. (28) and (29); however, a numerical solution is straightforward. A program in MATLAB (version 8.1) is written to implement the solution.

Table 1. Convergence characteristics for the dimensionless natural frequencies (γ = 5).

Modes number	Dimensionless natural frequencies, ω_n					
	ω_1	ω_2	ω_3	ω_4	ω_5	ω_6
1	13.706	20.170	-	-	-	-
2	13.207	19.956	41.615	59.221	-	-
3	13.201	19.948	41.103	58.711	84.074	118.13
4	13.181	19.942	41.096	58.689	83.470	116.82
5	13.176	19.942	41.086	58.685	83.461	116.76
6	13.171	19.940	41.082	58.685	83.453	116.75
7	13.170	19.940	41.079	58.684	83.449	116.75
8	13.169	19.940	41.077	58.683	83.447	116.75
9	13.168	19.939	41.076	58.683	83.445	116.75
10	13.168	19.939	41.075	58.683	83.443	116.75

3. Verification of the modeling method

In the numerical calculations of the present study, unless special description, the dimensionless parameters are set as: Ψ = 10°, Θ = 30°, κ = 0.5, μ = 900, δ = 1, ε_T= 5e-4.

Convergence tests for the natural frequencies are used to evaluate the suitability of the base functions for the displacement variables. The convergence characteristics of the first six dimensionless natural frequencies are listed in Table 1. It is observed that the natural frequencies converge when the truncation modes number approaches 10. Thus, the first ten shape functions are applied to solve the eigenvalue problem to achieve accurate results in further computations.

In the present study, three Cartesian variables are employed to describe the elastic deformation of the rotating beam. The accuracy of this modelling method is examined by comparing with the hybrid variables method [32, 36, 37]. In these references, the hybrid variables method was successfully applied to a rotating cantilever beam. To verify the present modelling method with previous references, the mode shape functions are replaced with those of the cantilever beam, and the axial inertial force is changed to following expression for the clamped-free boundary condition:

$$F_P = \frac{1}{2}\rho A\Omega^2(L^2 - x^2) + \rho A\Omega^2 r(L - x). \tag{30}$$

Other parameters are chosen as Ψ = 0°, Θ = 0°, κ = 1, δ = 0, ε_T = 0 following the Ref. [36]. The first two dimensionless natural frequencies in the flapwise vibration under different rotating speed obtained by two modelling methods are displayed in Table 2. The numerical result shows the present modelling method has a good agreement with previous research.

The present discretized motion equations are also verified by comparing with a commercial FEM code, ANSYS. The pretwisted beam is divided into 3D solid elements. Fig. 3 shows a typical finite element mesh. The dimensional parame-

Table 2. Comparison of first two dimensionless flapwise natural frequencies ($\Psi = 0°$, $\Theta = 0°$, $\kappa = 1$, $\delta = 0$, $\varepsilon_T = 0$).

Rotating speed ratio	First natural frequency		Second natural frequency	
	Present	Ref. [36]	Present	Ref. [36]
0	3.5160	3.5160	22.034	22.035
1	3.6816	3.6816	22.181	22.181
2	4.1373	4.1373	22.615	22.615
3	4.7972	4.7973	23.320	23.320
4	5.5849	5.5850	24.273	24.273
5	6.4495	6.4495	25.445	25.446
6	7.3603	7.3604	26.808	26.809
7	8.2997	8.2996	28.332	28.334
8	9.2570	9.2568	29.993	29.995
9	10.226	10.226	31.768	31.771
10	11.203	11.202	33.638	33.640

Table 3. Material properties and geometric parameters used in FEM.

Notation	Description	Value
E	Young's modulus of the material	7e10 N/m^2
ρ	Density of the material	2800 kg/m^3
α	Coefficient of thermal expansion	2.5e-5 /℃
Ψ	Stagger angle	10°
Θ	Pretwist angle	30°
L	Length	30 m
w	Width	1 m
h	Height	0.707 m
r	Radius of the hub	30 m
Ω	Rotating speed	3.208 rad/s
ΔT	Environment temperature rise	0, 20, 40, 60℃

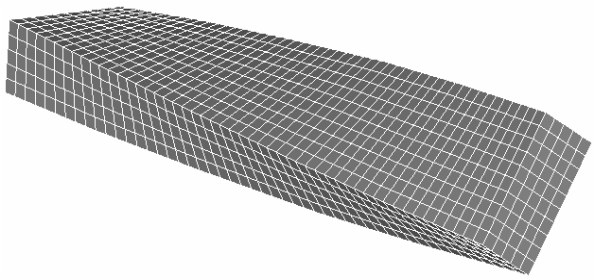

Fig. 3. A typical finite element mesh of a pretwisted beam.

ters used in finite element analysis are listed in Table 3. In light of Eq. (25), one can easily find that the dimensionless rotating speed is $\gamma = 2$ and other dimensionless parameters are same as those described before. In the finite element analysis, a static problem including the rotating motion and thermal environment is initially conducted, and then the produced stress field is considered in the subsequent mode analysis. Table 4 lists the first three dimensionless natural frequencies under different environment temperatures obtained by present method and FEM. The maximum difference between them is less than 1%.

Table 4. First three dimensionless natural frequency obtained by the present method and FEM ($\gamma = 2$).

ε_T	Mode	Theory	FEM	Error (%)
0	1st	16.006	16.000	0.035
	2nd	22.009	21.888	0.548
	3rd	44.135	43.966	0.384
5.0E-4	1st	13.748	13.749	0.007
	2nd	20.433	20.312	0.592
	3rd	41.207	41.044	0.396
1.0E-3	1st	10.989	10.998	0.086
	2nd	18.708	18.585	0.656
	3rd	38.040	37.882	0.416
1.5E-3	1st	7.1589	7.1837	0.347
	2nd	16.784	16.657	0.757
	3rd	34.568	34.413	0.447

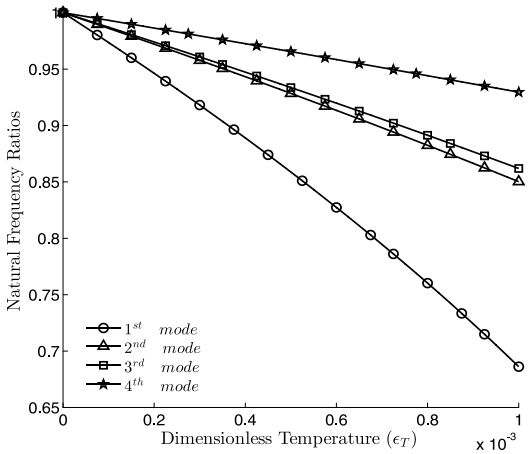

Fig. 4. The effect of thermal environment on the natural frequencies of beam ($\gamma = 2$).

From the convergence tests and the comparison with previous report and commercial finite element code, the accuracy of the present model is validated.

4. Numerical investigation

The effects of thermal stress on the natural frequencies are plotted in Fig. 4. Here, the natural frequency reduction is defined as $\omega_i^{\Delta T}/\omega_i^0$, where $\omega_i^{\Delta T}$ is the ith dimensionless natural frequency of the rotating beam under the thermal environment, and ω_i^0 is corresponding dimensionless one without the thermal effect. The result shows a nearly linear decrement of natural frequencies with the dimensionless temperature. In addition, the reduce rate is strangest for the first natural frequency, and tends to decay for higher order ones. For the present case, the variation of second natural frequency is close to that of the third one. In fact, under thermal environment, there exists a uniform compressive thermal stress field throughout the beam, which results in a softening effect on the rotating

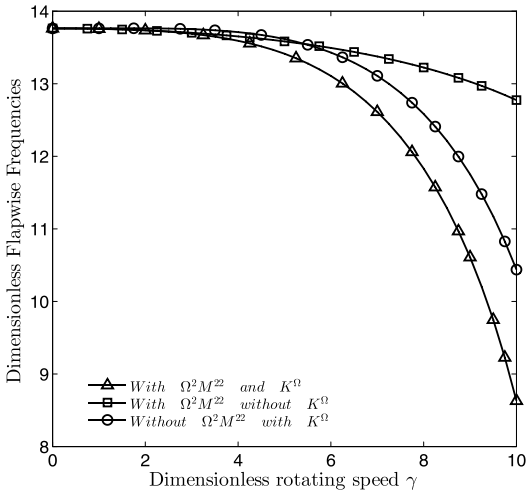

(a)

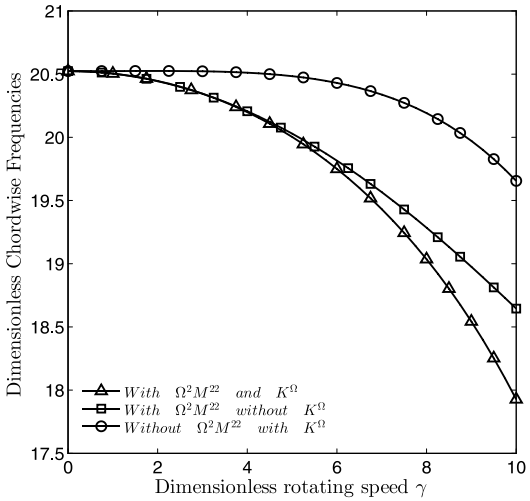

(b)

Fig. 5. Study of spin softening and axial stress effects on the natural frequencies: (a) Flapwise frequencies; (b) chordwise frequencies.

clamped beam.

The variation of first two dimensionless natural frequencies with the rotating speed is illustrated in the Fig. 5. The spin softening term does not appear explicitly in the flapwise component (see Eq. (22)). However, nonzero pretwist angle and stagger angle introduce the coupling effect between flapwise vibration and chordwise vibration. As a result, the spin softening term in chordwise component will decrease the flapwise natural frequency (see Fig. 5(a)). If the rotating speed is high enough, the softening effect due to axial stress seems to be more significant than the spin softening for the flapwise frequency. From Fig. 5(b), the spin softening is dominant in chordwise frequency for a wide range of rotating speed. The axial stress effects seem to soften the rotating clamped beam in both the flapwise and chordwise vibration. This is different from the case of cantilever beam reported in previous papers. In fact, the axial force Eq. (15) is not always positive along the

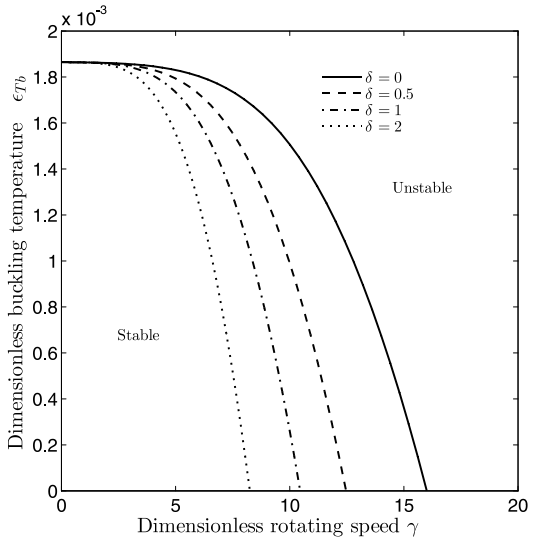

Fig. 6. The variation of the Buckling temperature with rotating speed.

neutral axis of the rotation beam. For the clamped rotating beam, the tensile stress distributes only on the span $[0, \chi_0]$, in which $\chi_0 = -\delta + \sqrt{\delta^2 + \delta + \frac{1}{3}}$. However, the rest of the beam is under compressive stress. Fig. 5 proves that the softening effect due to the compressive stress is greater than the stiffening effect due to the tensile stress.

The variation of the buckling temperature with rotating speed for different hub radii is shown in Fig. 6. It is obvious that rotating motion decreases the buckling temperature. For larger hub radius, the softening effect due to the axial stress is more significant, so the corresponding stable region is reduced. For present case, the curves joint at the same value of 1.86e-3, when the rotating speed approaches to zero. The increment in rotating speed magnifies the difference of buckling temperature for different hub radii. The effects of thermal environment on the critical rotating speed γ_c are illustrated in Fig. 7. With the growth of environment temperature, the curves decline and converge to the same point, which just represents the thermal buckling status of the non-rotating pretwisted beam, with the value of 1.86e-3 as the previous case.

The effects of hub radius on the buckling rotating speed and critical rotating speed for different pretwist angles are discovered in Figs. 8 and 9, respectively. It is seen that γ_b decreases as δ increases. In particular, buckling rotating speed decreases sharply for small values of radius ratio. In addition, for small radius ratio, a larger pretwist angle could result in a lower buckling rotating speed. However, for large radius ratio, the difference in γ_b is shrunk for different pretwist angles. In fact, when the radius ratio is large enough, the stiffness $K^{\Omega i}$ (A.7) due to centrifugal stress effect becomes dominant in the total stiffness matrix and the effect of the pretwist angle, Eqs. (A.3)-(A.5), becomes negligible. The variation characteristics of critical rotating speed are quite similar to those of buckling rotating speed.

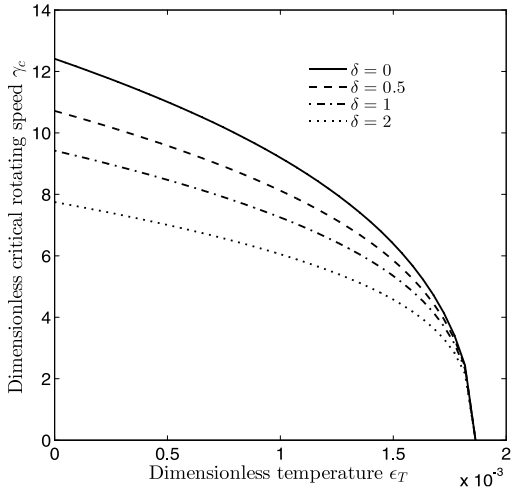

Fig. 7. The influence of thermal environment on the critical rotating speed.

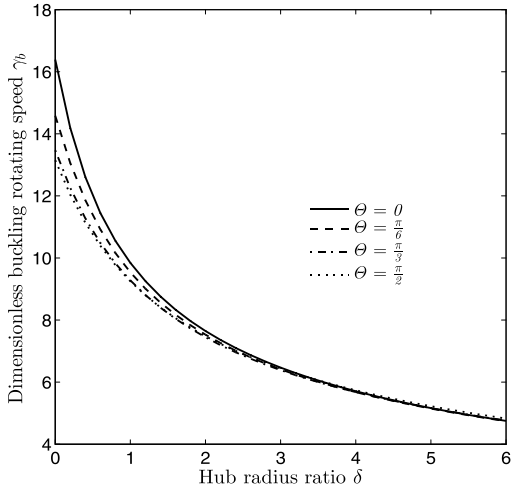

Fig. 8. The variation of the buckling rotating speed with hub radius under thermal stress.

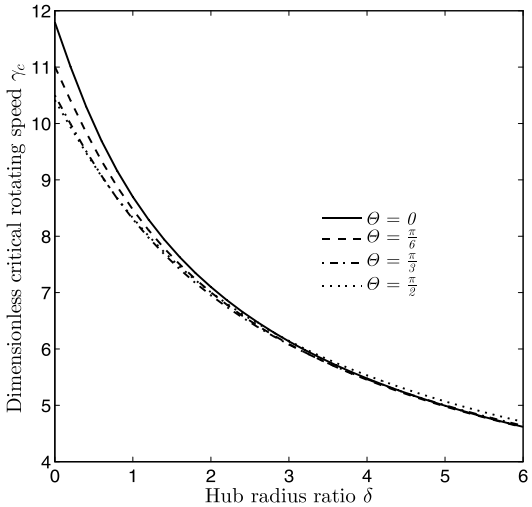

Fig. 9. The variation of the critical rotating speed with hub radius under thermal stress.

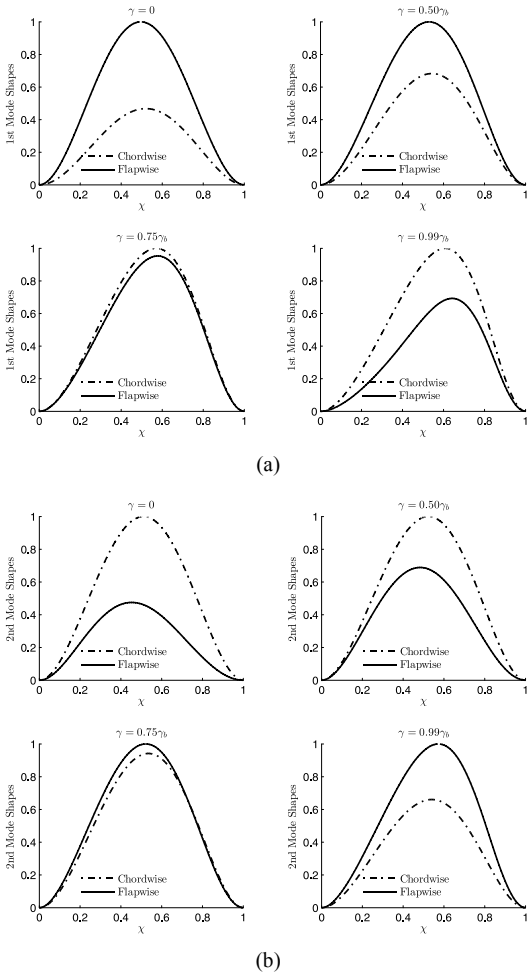

Fig. 10. First two mode shapes for different rotating speeds ($\delta = 0$, $\varepsilon_T = 0$): (a) First mode shape; (b) second mode shape.

Fig. 10 displays the first two mode shapes for different rotating speeds (0, $0.5\gamma_b$, $0.75\gamma_b$, $0.99\gamma_b$, in which γ_b =16.005 for present case). The coupling effects between the chordwise vibration and flapwise vibration, which are introduced by non-zero pretwist angle and stagger angle, could be observed. With the improvement of rotating speed, these coupling effects are magnified. The dominant mode shapes in the two components even switch each other for some cases. To observe the effect of rotating speed on the mode shapes, the normalized chordwise mode shapes are put together and plot in Fig. 11. The variation in flapwise mode shapes, which are not displayed here, is similar to that of chordwise mode shapes. It is obvious that with the growth of rotating speed, the peak value position of the mode shape moves to the tip end of the rotating beam, and the movement rate increases with the rotating speed rapidly. Physically, both the tensile stress near the root end and compressive stress near the tip end are improved with the increment of the rotating speed. So the root end part is stiffened; however, the tip end part is softened at the same time. As a result, the peak value position will move to the softening part.

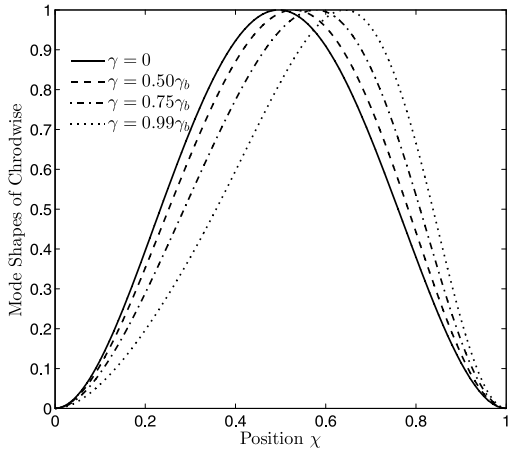

Fig. 11. Normalized chordwise mode shapes for different rotating speeds.

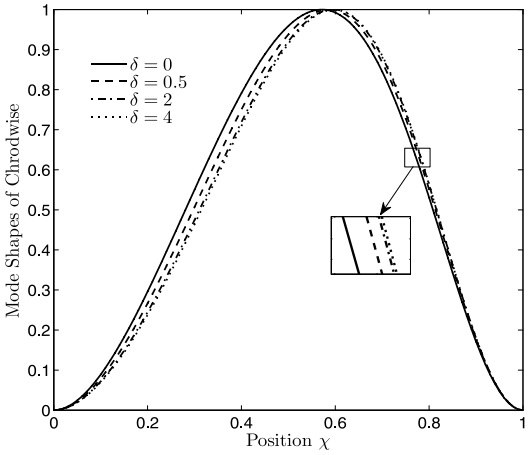

Fig. 13. Normalized chordwise mode shapes for different hub radii.

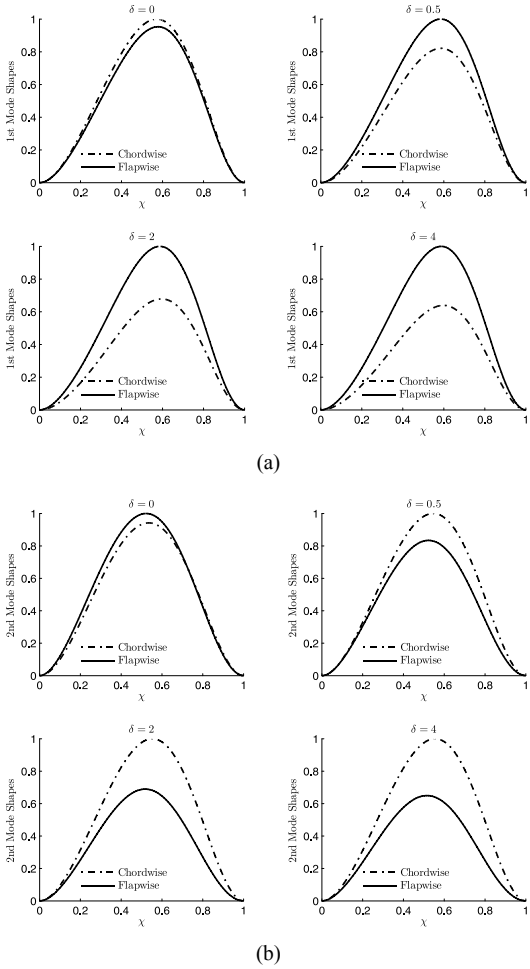

Fig. 12. First two mode shapes for different hub radii ($\gamma = 0.75\gamma_b$, $\underline{\varepsilon_T} = 0$): (a) First mode shape; (b) second mode shape.

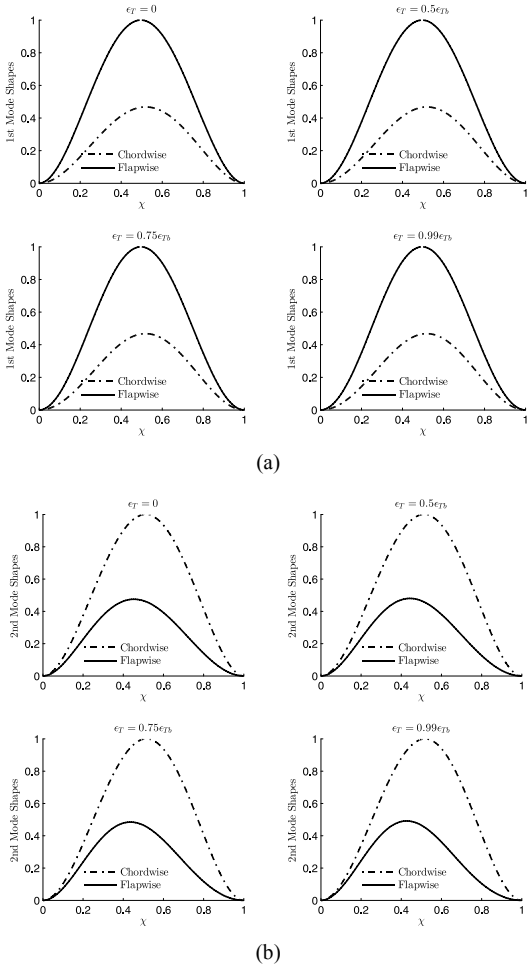

Fig. 14. First two mode shapes for different environment temperatures: ($\delta = 0$, $\gamma = 0$): (a) First mode shape; (b) second mode shape.

Similarly, the influence of the hub radius δ on the mode shapes is discovered in Figs. 12 and 13. The rotating speed is set as three quarter of buckling rotating speed for each case (for $\delta = 0$, $\gamma_b = 16.005$; $\delta = 0.5$, $\gamma_b = 12.469$; $\delta = 2$, $\gamma_b = 8.254$ and when $\delta = 4$, $\gamma_b = 6.220$). The exchange in mode shapes could also be observed in present cases. In addition, a slight movement of the peak value position is revealed. The movement rate decreases with hub radius ratio, hence the mode shapes seem to converge to a certain shape as the growth of δ. In fact, when the hub radius δ increases from 0 to ∞, the

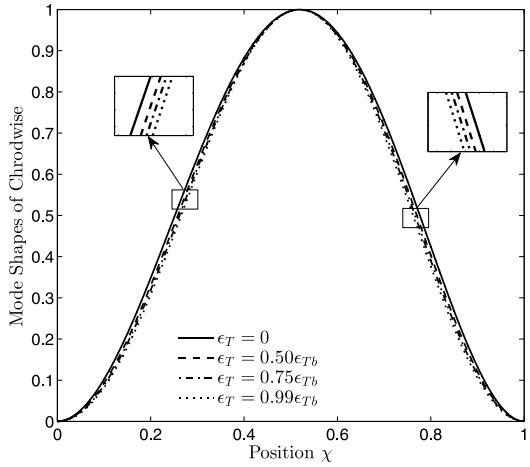

Fig. 15. Normalized chordwise mode shapes for different environment temperature.

division point χ_0, which divides the tensile part from the compressive part, will approach to $1/2$ from $1/\sqrt{3}$. So the compressive stress zone is extended, and the peak value position approaches to the tip end.

Finally, the influence of thermal environment on the mode shapes is studied in Figs. 14 and 15. Four typical temperatures (0, $0.5\varepsilon_{Tb}$, $0.75\varepsilon_{Tb}$ and $0.99\varepsilon_{Tb}$, in which ε_{Tb} = 1.86e-3) are adopted as thermal environment. Nether the transformation in mode shapes nor the movement of the peak value position could be observed in the present cases. However, the only variation is that the mode shapes seem to become a little "thinner" when the temperature is increased. In the present study the temperature field along the beam is assumed to be uniform, so the axial stress is decreased uniformly along the beam when the temperature is increased. As a result, the peak value position would not move for different environment temperature.

5. Conclusion

Equations of motion for rotating pretwisted clamped-clamped beam under thermal stress were derived by employing three pure Cartesian deformation variables combined with nonlinear von Karman strain. The geometric complexities of the rotating blade, such as pretwist angle and stagger angle, were considered. The effects of thermal environment, rotating speed, the hub radius and pretwist angle on the dynamic characteristics of rotating pretwisted clamped beam were investigated through numerical study. Numerical results obtained with the present modeling method are in good agreement with the previous results reported in the literature and the results calculated from a commercial finite element code. Both the thermal environment and rotation motion show a softening effect on the rotating clamped beam. The influence of pretwist angle and hub radius on the buckling rotating speed and critical rotating speed was discovered. The coupling effects between the mode shapes for chordwise vibration and flapwise vibration introduced by the pretwist angle and stagger angle could be magnified by the rotating speed. The exchange in mode shapes can be observed in some cases. The increment in the rotating speed and the hub radius could move the peak value position of the mode shape to the tip end of the beam; however, the variation in temperature will not. It seems that the first mode shape will become a little "thinner" with the increment of environment temperature. Some related physical explanations are discussed in the present paper.

Acknowledgment

This work is supported by the National Basic Research Program of China [No.2013CB035704]; the National Nature Science Foundation of China [No.11472206]; Hong Kong RGC-GRF Grant [Projects No. CityU 118212] and Strategic research grant, City University of Hong Kong [Projects No. CityU-SRG 7004176].

References

[1] J. S. Rao, *Turbomachine blade vibration,* New Age International (1991).

[2] A. R. Sahu, Theoretical frequency equation of bending vibrations of an exponentially tapered beam under rotation, *J. of Vibration and Control*, 7 (6) (2001) 775-780.

[3] H. H. Yoo, J. Y. Kwak and J. Chung, Vibration analysis of rotating pre-twisted blades with a concentrated mass, *J. of Sound and Vibration*, 240 (5) (2001) 891-908.

[4] M. N. V. Ramesh and N. M. Rao, Free vibration analysis of pre-twisted rotating fgm beams, *International J. of Mechanics and Materials in Design*, 9 (4) (2013) 367-383.

[5] M. T. Piovan and R. Sampaio, A study on the dynamics of rotating beams with functionally graded properties, *J. of Sound and Vibration*, 327 (1-2) (2009) 134-143.

[6] J. R. Banerjee, Free vibration of centrifugally stiffened uniform and tapered beams using the dynamic stiffness method, *J. of Sound and Vibration*, 233 (5) (2000) 857-875.

[7] J. R. Banerjee, Frequency equation and mode shape formulae for composite Timoshenko beams, *Composite Structures*, 51 (4) (2001) 381-388.

[8] J. R. Banerjee, H. Su and D. R. Jackson, Free vibration of rotating tapered beams using the dynamic stiffness method, *J. of Sound and Vibration*, 298 (4-5) (2006) 1034-1054.

[9] J. R. Banerjee and D. R. Jackson, Free vibration of a rotating tapered Rayleigh beam: A dynamic stiffness method of solution, *Computers & Structures*, 124 (2013) 11-20.

[10] S. M. Chu, D. Q. Cao, S. P. Sun, J. Z. Pan and L. G. Wang, Impact vibration characteristics of a shrouded blade with asymmetric gaps under wake flow excitations, *Nonlinear Dynamics*, 72 (3) (2013) 539-554.

[11] Y. J. Chiu and C. H. Yang, The coupled vibration in a rotating multi-disk rotor system with grouped blades, *J. of Mechanical Science and Technology*, 28 (5) (2014) 1653-1662.

[12] B. Zhang and Y. M. Li, Six degrees of freedom coupled

dynamic response of rotor with a transverse breathing crack, *Nonlinear Dynamics*, 78 (3) (2014) 1843-1861.

[13] I. A. Khan and D. R. Parhi, Fault detection of composite beam by using the modal parameters and RBFNN technique, *J. of Mechanical Science and Technology*, 29 (4) (2015) 1637-1648.

[14] M. H. Yao, Y. P. Chen and W. Zhang, Nonlinear vibrations of blade with varying rotating speed, *Nonlinear Dynamics*, 68 (4) (2012) 487-504.

[15] M. H. Yao, W. Zhang and Y. P. Chen, Analysis on nonlinear oscillations and resonant responses of a compressor blade, *Acta Mechanica*, 225 (12) (2014) 3483-3510.

[16] M. N. Hamdan and A. H. El-Sinawi, On the non-linear vibrations of an inextensible rotating arm with setting angle and flexible hub, *J. of Sound and Vibration*, 281 (1-2) (2005) 375-398.

[17] M. O. Kaya and O. O. Ozgumus, Energy expressions and free vibration analysis of a rotating uniform Timoshenko beam featuring bending-torsion coupling, *J. of Vibration and Control*, 16 (6) (2010) 915-934.

[18] G. Sakar and M. Sabuncu, Buckling and dynamic stability of a rotating pretwisted asymmetric cross-section blade subjected to an axial periodic force, *Finite Elements in Analysis and Design*, 40 (11) (2004) 1399-1415.

[19] H. P. Lee, Buckling and dynamic stability of spinning pretwisted beams under compressive axial loads, *International J. of Mechanical Sciences*, 36 (11) (1994) 1011-1026.

[20] V. K. Badagi and R. Ganesan, Vibration and buckling response of width tapered laminated composite beams using Ritz method for rotorcraft blade, *Proceedings of the ASME International Design Engineering Technical Conferences and Computers and Information in Engineering Conference* (2010) 799-816.

[21] Y. Fu, J. Wang and S. Hu, Analytical solutions of thermal buckling and postbuckling of symmetric laminated composite beams with various boundary conditions, *Acta Mechanica*, 225 (1) (2014) 13-29.

[22] A. Ranjbaran, M. R. Khoshravan and M. Kharazi, Buckling analysis of sandwich plate using layerwise theory, *J. of Mechanical Science and Technology*, 28 (7) (2014) 2769-2777.

[23] J. D. Johnston and E. A. Thornton, Thermally induced attitude dynamics of a spacecraft with a flexible appendage, *J. of Guidance Control and Dynamics*, 21 (4) (1998) 581-587.

[24] N. Saniei and A. C. J. Luo, Thermally induced, nonlinear vibrations of rotating disks, *Nonlinear Dynamics*, 26 (4) (2001) 393-409.

[25] D. C. D. Oguamanam, J. S. Hansen and G. R. Heppler, Nonlinear transient response of thermally loaded laminated panels, *J. of Applied Mechanics-Transactions of the ASME*, 71 (1) (2004) 49-56.

[26] J. Y. Liu and H. Lu, Nonlinear formulation for flexible multibody system applied with thermal load, *Proceedings of the ASME International Design Engineering Technical Conferences and Computers and Information in Engineering Conference* (2008) 1173-1181.

[27] J. S. Tomar and R. Jain, Effect of thermal-gradient on frequencies of a wedge-shaped rotating beam, *AIAA J.*, 22 (6) (1984) 848-850.

[28] J. S. Tomar and R. Jain, Thermal effect on frequencies of coupled vibrations of pretwisted rotating beams, *AIAA J.*, 23 (8) (1985) 1293-1296.

[29] O. Song, L. Librescu and S. Y. Oh, Dynamics of pretwisted rotating thin-walled beams operating in a temperature environment, *J. of Thermal Stresses*, 24 (3) (2001) 255-279.

[30] S. S. Na, L. Librescu and H. D. Jung, Dynamics and active bending vibration control of turbomachinery rotating blades featuring temperature-dependent material properties, *J. of Thermal Stresses*, 27 (7) (2004) 625-644.

[31] L. Librescu, S. Y. Oh, O. Song and H. S. Kang, Dynamics of advanced rotating blades made of functionally graded materials and operating in a high-temperature field, *J. of Engineering Mathematics*, 61 (1) (2008) 1-16.

[32] H. H. Yoo, J. H. Park and J. Park, Vibration analysis of rotating pre-twisted blades, *Computers & Structures*, 79 (19) (2001) 1811-1819.

[33] B. O. Al-Bedoor and Y. A. Khulief, General planar dynamics of a sliding flexible link, *J. of Sound and Vibration*, 206 (5) (1997) 641-661.

[34] A. A. Al-Qaisia and B. O. Al-Bedoor, Evaluation of different methods for the consideration of the effect of rotation on the stiffening of rotating beams, *J. of Sound and Vibration*, 280 (3-5) (2005) 531-553.

[35] Y. J. Chiu and D. Z. Chen, The coupled vibration in a rotating multi-disk rotor system, *International J. of Mechanical Sciences*, 53 (1) (2011) 1-10.

[36] H. H. Yoo and S. H. Shin, Vibration analysis of rotating cantilever beams, *J. of Sound and Vibration*, 212 (5) (1998) 807-828.

[37] S. Kwon, J. Chung and H. H. Yoo, Structural dynamic modeling and stability of a rotating blade under gravitational force, *J. of Sound and Vibration*, 332 (11) (2013) 2688-2700.

Appendix

A. Matrices in equations of motion

The matrices and their components in Eq. (22) are derived as:

$$M^{ij} = \int_0^L \rho A \phi_i^T \phi_j \mathrm{d}x \tag{A.1}$$

$$K^S = \int_0^L EA \phi_{i,x}^T \phi_{i,x} \mathrm{d}x \tag{A.2}$$

$$K^{B2} = \int_0^L EI_3 \phi_{2,xx}^T \phi_{2,xx} \mathrm{d}x \tag{A.3}$$

$$K^{B3} = \int_0^L EI_2 \phi_{3,xx}^T \phi_{3,xx} \mathrm{d}x \tag{A.4}$$

$$K^{Bij} = \int_0^L EI_{23} \phi_{i,xx}^T \phi_{j,xx} \mathrm{d}x \tag{A.5}$$

$$K^{Ti} = \int_0^L N_T \phi_{i,x}^T \phi_{i,x} \mathrm{d}x \tag{A.6}$$

$$K^{\Omega i}=\rho A\Omega^2\int_0^L\left[\frac{1}{6}\left(L^2-3x^2\right)+\frac{1}{2}r\left(L-2x\right)\right]\phi_{i,x}^T\phi_{i,x}\mathrm{d}x \quad (A.7)$$

$$Q_1=\int_0^L\rho A\Omega^2\left(r+x\right)\phi_i^T\mathrm{d}x+\int_0^L N_T\phi_{i,x}^T\mathrm{d}x \quad (A.8)$$

$$Q_2=-\int_0^L M_{Tz}\phi_{2,xx}^T\mathrm{d}x \quad (A.9)$$

$$Q_3=-\int_0^L M_{Ty}\phi_{3,xx}^T\mathrm{d}x\,. \quad (A.10)$$

The dimensionless matrices and elements in Eq. (26) are written as followings.

$$\bar{\mathbf{M}}=\begin{bmatrix}\bar{M}^{22} & 0\\ 0 & \bar{M}^{33}\end{bmatrix} \quad (A.11)$$

$$\bar{\mathbf{K}}=\begin{bmatrix}\bar{K}^{B2}-\gamma^2\bar{M}^{22}+\bar{K}^{\Omega 2}-\bar{K}^{T2} & \bar{K}^{B23}\\ \bar{K}^{B32} & \bar{K}^{B3}+\bar{K}^{\Omega 3}-\bar{K}^{T3}\end{bmatrix} \quad (A.12)$$

$$\bar{M}^{ij}=\int_0^1\varphi_i^T\varphi_j\mathrm{d}\chi \quad (A.13)$$

$$\bar{K}^{B2}=\int_0^1\left[\frac{\kappa+1}{2}-\frac{\kappa-1}{2}\cos\left[2\left(\Theta\chi+\Psi\right)\right]\right]\varphi_{2,\chi\chi}^T\varphi_{2,\chi\chi}\mathrm{d}\chi \quad (A.14)$$

$$\bar{K}^{B3}=\int_0^1\left[\frac{\kappa+1}{2}+\frac{\kappa-1}{2}\cos\left[2\left(\Theta\chi+\Psi\right)\right]\right]\varphi_{3,\chi\chi}^T\varphi_{3,\chi\chi}\mathrm{d}\chi \quad (A.15)$$

$$\bar{K}^{Bij}=\int_0^1\left[\frac{\kappa-1}{2}\sin\left[2\left(\Theta\chi+\Psi\right)\right]\right]\varphi_{i,\chi\chi}^T\varphi_{j,\chi\chi}\mathrm{d}\chi \quad (A.16)$$

$$\bar{K}^{Ti}=12\mu\varepsilon_T\int_0^1\varphi_{i,\chi}^T\varphi_{i,\chi}\mathrm{d}\chi \quad (A.17)$$

$$\bar{K}^{\Omega i}=\gamma^2\int_0^1\left[\frac{1}{6}\left(1-3\chi^2\right)+\frac{1}{2}\delta\left(1-2\chi\right)\right]\varphi_{i,\chi}^T\varphi_{i,\chi}\mathrm{d}x. \quad (A.18)$$

Bo Zhang received his B.S. in Engineering Mechanics from Xi'an Jiao Tong University in 2011. He is a Ph.D. candidate at State Key Laboratory for Strength and Vibration of Mechanical Structures, Xi'an Jiaotong University. His research interests include rotor dynamics and nonlinear vibrations of structures.